RSC Advances

PAPER

View Article Online
View Journal | View Issue

Cite this: *RSC Adv.*, 2025, **15**, 4443

Highly efficient hydrogenation of furfural to furfuryl alcohol over Cu–Al_2O_3–ZnO catalyst†

Junqi Zhang, Yongwang Li, Zhiwei Zhang, Zheng Wang, Jiaxing Zhang, Shuai Liu, Yang Qin, Bingxin Zhu, Tongxue Zhang, Hongyu Wang, Fumin Wang * and Xubin Zhang *

Received 6th December 2024
Accepted 2nd February 2025

DOI: 10.1039/d4ra08609k

rsc.li/rsc-advances

The development of simple, efficient and economical catalysts for the hydrogenation of biomass to produce high value-added chemicals is of great significance in solving the energy crisis. In this work, a series of non-precious metal catalysts (Cu–Al_2O_3–ZnO) with different defect sites were prepared by etching Devarda's alloy. Under optimized mild reaction conditions, the furfural conversion and furfuryl alcohol selectivity are both greater than 99.0%, and the catalyst has good reusability. Characterisation and experiments were used to investigate the activate species for hydrogenation reaction. It can be proved that the low-valent Cu species in the Cu–Al_2O_3–ZnO catalysts play an important role as adsorption and dissociation sites for H_2. Different etching degrees and sample reduction temperatures of the alloy can be used to adjust the content of acidic sites such as Al_2O_3 and CuO, which have appropriate adsorption properties for furfural. ZnO promotes the dispersion of the Cu species and enhances the accessibility of the active sites. The etching method achieves the interaction between species to further enhance the stability and activity of the catalyst. The catalytic performance of the catalyst is very competitive and this study provides a new method for the efficient hydrogenation of furfural to furfuryl alcohol.

1. Introduction

In the context of fossil fuel depletion and global warming, the extraction of high value-added products from a wide range of biomass platform chemicals has gradually become a viable alternative to petroleum products in order to solve a range of environmental problems and the energy crisis, and to reduce over-reliance on fossil fuels.[1–3] Furfural (FAL) derived from lignocellulosic biomass, has attracted increasing attention in recent years as a valuable platform chemical that can be used as an intermediate to provide a variety of products for the energy, chemical and pharmaceutical industries,[4,5] furthermore, in the hydrogenation reaction, due to the presence of various unsaturated groups (C=C, C=O) in the FAL molecule, a wide range of products can be produced, such as furfuryl alcohol (FOL), tetrahydrofurfuryl alcohol, 2-methylfuran, 2-methyltetrahydrofuran, 1,2-pentanediol and 1,5-pentanediol.[6–10]

Catalytic hydrogenation has been used as the main application for the conversion of FAL to various high-value chemicals. The majority of FAL worldwide (~65%) are used in the production of FOL.[11] FOL is considered a high-value intermediate that can be used as a raw material to manufacture products such as vitamin C and lysine,[12,13] and has a wide range of applications in the fields of polymers, pharmaceuticals and cosmetics.[12–14] Generally speaking, the C=C bond is active, and the FOL can further hydrogenate the C=C bond to form tetrahydrofurfuryl alcohol.[15,16] In addition, hydrolysis of the FOL moiety can produce other by-products, resulting in a variety of complex and competing reaction pathways.[17] Since excessive hydrogenation or hydrolysis produces other by-products, which is the main problem with the hydrogenation of FAL to FOL, it is necessary to ensure high hydrogenation activity while preferentially hydrogenating C=O groups and avoiding excessive hydrogenation.

At present, various transition metal catalysts are often used for the selective hydrogenation of FAL to FOL. In general, precious metal catalysts tend to have higher catalytic activity than non-precious metal catalysts, and they are often used in combination with non-precious metal elements to catalyze hydrogenation reactions. For example, precious metal elements Pt, Ru and Pd-based catalysts[18–21] exhibit high activity in the hydrogenation of FAL to FOL under relatively mild reaction conditions (30–100 °C, 0.8–2 MPa H_2). However, factors such as the high cost of precious metal catalysts and the difficulty of recycling also severely limit their large-scale practical application. Compared to precious metal catalysts, Ni, Co and Cu-based non-precious metal catalysts have also achieved high

School of Chemical Engineering and Technology, Tianjin University, Tianjin 300350, China. E-mail: tjzxb@tju.edu.cn

† Electronic supplementary information (ESI) available. See DOI: https://doi.org/10.1039/d4ra08609k

FAL conversion rates and high FOL yields in the hydrogenation of FAL to FOL. For example, CuCo/MgO,[11] Cu–ZnO–Al_2O_3,[22] $Cu_2Ni_1AlO_y$,[23] CoAl,[24] C@Ni_3P[25] have achieved more than 95% yields of FOL. However, some non-precious metal catalysts also have the disadvantages of complicated preparation process and low reactivity. Among the non-precious metal catalysts, the transition metal Cu initially adsorbs preferentially on the C=O of FAL rather than the furan ring due to the overlap of the 3d band of Cu atoms with the antibonding orbitals of the furan ring, which is highly selective for FOL.[26–30] However, the interaction between monometallic Cu-based catalysts and FAL is generally weak, the accessibility of the active center is severely restricted, and the reaction conditions for Cu-based catalysts have been relatively harsh in the past.[31,32] Therefore, enhancing the interaction between Cu-based catalysts and FAL and improving catalytic activity are the main issues that need to be addressed in the hydrogenation of FAL to FOL.

Inspired by the widespread application and high activity of skeletal Cu-based catalysts derived from etched alloys in hydrogenation reactions,[33–36] as well as the versatility of RANEY® nickel[37,38] and etched alloy[39–41] catalysts in hydrogenation processes, we explored the potential of Devarda's alloy (CuAlZn) as an ideal catalyst for the selective hydrogenation of FAL to FOL. In our study, skeletal Cu-based catalysts were prepared by etching Al and Zn from the Devarda's alloy using alkaline solutions of varying concentrations. These catalysts were subsequently applied to the hydrogenation of FAL, demonstrating their effectiveness in achieving selective and efficient production of FOL. The analysis shows that during the etching process of the alloy, some $Al(OH)_3$ would be formed and remains in the Cu skeleton. After high-temperature calcination and reduction, the unetched Al and the $Al(OH)_3$ remaining in the skeleton are oxidized and dehydrated to form amorphous Al_2O_3, which provide acidic sites for the adsorption of FAL. Meanwhile, the highly dispersed low-valent Cu species in the catalyst provide sites for H_2 adsorption and dissociation. The synergistic effect of the low-valent Cu species and the acidic sites enhance the activity of hydrogenation of FAL to FOL. The optimal catalytic performance of the catalysts depends on the ratio between the low-valent metal sites and the acidic sites. Meanwhile, the catalyst prepared by alloy etching method can make the Cu species more dispersed to enhance the accessibility of the active sites, and ZnO can further disperse the Cu species. The interactions among Al_2O_3, ZnO and Cu species in the samples can help to bring out the synergistic effect between the hydrogenation sites and the acidic sites and make the catalysts more structurally stable, with stronger catalytic activity, and the catalysts also have good reusability.

2. Experimental

2.1 Materials

FAL (>99.5%) and Devarda's alloy particles (M27196) were purchased from Morell (Shanghai) Chemical Technology Co., Ltd FOL (>99.0%), γ-Al_2O_3, $Cu(NO_3)_2\cdot 3H_2O$ (99.0%) and $Zn(NO_3)_2\cdot 6H_2O$ (99.0%) were purchased from Aladdin Reagent (Shanghai) Co., Ltd NaOH (AR) and ethanol (AR) were purchased from Tianjin Jiangtian Chemical Co., Ltd H_2 gas (purity 99.99%) and hydrogen–argon gas mixture (10 vol% H_2/Ar) were purchased from Tianjin Liufang Industrial Gas Co., Ltd.

2.2 Catalyst synthesis

The desired catalyst was synthesised using the etching method. In a typical synthesis, 2.0 g of Devarda's alloy (CuAlZn) particles were placed in 15.0 g of distilled water and stirred, named Sample A. Then, 15.0 g of 10 wt% NaOH solution was prepared, named Solution B. During stirring at a constant temperature of 25 °C, Solution B was added dropwise to Solution A to etch the alloy, and stirring lasted 11 h while the temperature was maintained at 25 °C. The precipitate was washed and centrifuged to the solution pH of about 7. The sample was dried in a vacuum oven at 60 °C overnight to obtain a powder sample. The dried sample was heated in a muffle furnace at 4 °C min^{-1} up to 400 °C, held for 3 h. After cooling, the sample was transferred to a tube furnace and heated at 3.8 °C min^{-1} up to 200 °C (reduction temperature), held for 3 h (10 vol% H_2/Ar), to obtain the $CAZ_{1.5/2.0}$-200 catalyst ($CAZ_{x/y}$-*M*: C stands for Cu, A stands for Al, Z stands for Zn, *x*/*y* stands for the mass ratio of NaOH to CuAlZn alloy, and *M* stands for the reduction temperature). The same process was used to prepare $CAZ_{1.0/2.0}$-200, $CAZ_{1.5/2.0}$-0, $CAZ_{1.5/2.0}$-100, $CAZ_{1.5/2.0}$-200, $CAZ_{1.5/2.0}$-300, $CAZ_{2.0/2.0}$-200 and $CAZ_{2.5/2.0}$-200 catalysts with different reduction temperatures and etching concentrations, and were compared in terms of their performance.

Cu/Al_2O_3 was synthesized by the traditional impregnation method, in which Cu (35 wt% of γ-Al_2O_3) was loaded on γ-Al_2O_3. A 35% Cu/Al_2O_3 catalyst was prepared by dissolving a certain amount of $Cu(NO_3)_2\cdot 3H_2O$ in deionised water, then slowly dropping the Cu solution into a solution sample containing the γ-Al_2O_3 support while stirring, leaving it to stand for 12 h, drying in an oven at 120 °C for 12 h. The dried sample was heated in a muffle furnace at 4 °C min^{-1} up to 400 °C, held for 3 h. After cooling, the sample was transferred to a tube furnace and heated at 3.8 °C min^{-1} up to 200 °C, held for 3 h (10 vol% H_2/Ar) to obtain the 35%Cu/Al_2O_3 catalyst. The process for preparing $ZnO/Cu/Al_2O_3$ was the same as that for preparing Cu/Al_2O_3, except that a certain amount of $Cu(NO_3)_2\cdot 3H_2O$ and $Zn(NO_3)_2\cdot 6H_2O$ (1.33 wt% Zn of γ-Al_2O_3) were dissolved together in deionised water to produce the final catalyst 1.33% ZnO/35%Cu/Al_2O_3. The performance of these catalysts was compared.

2.3 Catalytic test conditions

The reaction was carried out in a 200 mL autoclave with a mechanical stirring speed of 600 rpm. Firstly, the ethanol solvent (60.0 g), FAL (1.20 g) and a certain amount of catalyst powder were added to the autoclave. Before each run, the vessel was sealed and the air in the vessel was replaced with 1.0 MPa N_2 four times. Then H_2 was introduced at the corresponding pressure, and the reactor was heated to a certain temperature with vigorous stirring. The reaction time was started when the temperature reached the predetermined value. After the

reaction was completed, the reactor was allowed to cool down by itself. In the catalyst cycle stability test, the reaction solution was centrifuged after each reaction to recover the catalyst. The recovered catalyst was thoroughly washed with ethanol three times in sequence, and then the catalyst was dried in a vacuum oven at 60 °C for 12 h for the next reaction. Before the reaction, it was heated in a muffle furnace at 4 °C min^{-1} up to 400 °C, held for 3 h. After cooling, the catalyst was transferred to a tube furnace and heated at 3.8 °C min^{-1} up to 200 °C, held for 3 h (10 vol% H_2/Ar). During the recovery process, about 10–15% of the catalyst was lost by weight, and the loss was compensated for by supplementing the recovery experiment with fresh catalyst (before each reaction, the quantities of catalyst, reactants, and solvent were standardised).

The product filtrate was analysed using a Beifen Ruili GC-3420A equipped with a FID detector and a capillary column (KB-Wax, 30 m × 0.32 mm × 0.5 μm, Kromat Corporation). The estimated experimental error was less than ±5% in all activity tests and the FAL conversion and selectivity and the product yield were calculated using the following eqn (1), (2) and (3).

$$C_{FAL} = \frac{M_{FAL}}{I_{FAL}} \times 100\% \quad (1)$$

$$S_i = \frac{M_i}{M_{FAL}} \times 100\% \quad (2)$$

$$Y_i = C_{FAL} \times S_i \quad (3)$$

where C_{FAL} represents the conversion of FAL after the reaction, M_{FAL} represents the molar amount of FAL consumed in the reaction, I_{FAL} represents the initial molar amount of FAL, S_i represents the selectivity towards the product, i represents the product, M_i represents the molar amount of the product, and Y_i represents the yield of the product. The carbon balance of all reactions in this study is higher than 94%.

2.4 Catalyst characterisation

The specific surface area was measured by using SSA-7000 (BET) low-temperature N_2 adsorption/desorption device. All samples were degassed at 150 °C for 4 h, and then adsorption and desorption were measured at −196 °C. X-ray diffraction (XRD) measurement was carried out on a Bruker D8 ADVANCE X-ray using Cu-Kα for crystallinity in the 2θ range of 10°–80° at a scanning speed of 8° min^{-1} to measure the catalyst precursors with different degrees of etching and the calcined reduced catalysts, and the energy dispersive spectroscopy was analysed by field emission scanning electron microscope (Apreo S LoVac-EDS). The sample was measured by field emission transmission electron microscopy (TEM) JEMF200. The surface functional groups of the samples were determined by Fourier Transform Infrared Spectroscopy (FT-IR) on a Nicolet-380 instrument with a DTGS detector. X-ray photoelectron spectroscopy (XPS) measurements were performed using K-Alpha+ from Thermo Fisher Scientific. The analysis was calibrated using the C 1s standard binding energy (284.8 eV). The catalyst with different etching concentrations at the same reduction temperature was measured by inductively coupled plasma optical emission spectrometry (ICP-OES, Agilent 725 ES & Agilent 5110). Ammonia Temperature-Programmed Desorption (NH_3-TPD) test was measured on a TP-5080-B instrument. The sample was pretreated at 150 °C in a helium atmosphere for 1 h. After cooling to 50 °C, a 10% NH_3/He mixture was injected to saturation, and then the He gas flow was switched to purge for 1 h to remove the weak physical adsorption NH_3 on the surface. Finally, the temperature was increased in a He atmosphere at 10 °C min^{-1} to 700 °C, and the removed gas was detected using a TCD. The Hydrogen Temperature-Programmed Desorption (H_2-TPD) test was measured on a TP-5080-B instrument. The sample was pretreated in a helium atmosphere at 150 °C for 1 h. After cooling to 50 °C, it was saturated with a 10% H_2/He mixture, and then purged with He gas for 1 h to remove the weak physical adsorption H_2 on the surface. Finally, the temperature was increased to 700 °C in a He atmosphere at 10 °C min^{-1} to 700 °C, and the removed gas was detected using a TCD. Pyridine-Infrared (Py-IR) test was measured on a Bruker Tensor 27 at 150 °C, 200 °C and 350 °C. The sample was evacuated at 350 °C for 1 h to remove impurity gases, then cooled naturally to 25 °C. Subsequently, the sample was vaporized with pyridine for 30 min, evacuated to 150 °C/200 °C/350 °C for 30 min. The spectra were taken at 25 °C.

3. Results and discussion

A series of Cu-based skeleton catalysts $CAZ_{0.5/2.0}$-200, $CAZ_{1.0/2.0}$-200, $CAZ_{1.5/2.0}$-200, $CAZ_{2.0/2.0}$-200, and $CAZ_{2.5/2.0}$-200 with different degrees of etching were successfully synthesized to explore the effect of different component content ratios on the performance of the catalyst. The influence of the reduction temperature was explored by using the $CAZ_{1.5/2.0}$-100/200/300 catalyst (optimum etch level catalysts), and the cyclic reusability of the catalyst was explored by using $CAZ_{1.5/2.0}$-200 as the experimental object.

3.1 Characterisation of $CAZ_{x/2.0}$-200

3.1.1 N_2 adsorption–desorption results. The surface area and pore size distribution of $CAZ_{x/2.0}$-200 catalysts with different degrees of etching were analysed using N_2 adsorption–desorption analysis. The result (Fig. 1A) shows that the isotherms of the samples $CAZ_{x/2.0}$-200 with low etching degree all exhibit typical type II isotherm shapes, and as the etching degree increases, the samples $CAZ_{2.0/2.0}$-200 and $CAZ_{2.5/2.0}$-200 exhibit type III isotherm shapes, indicating that the adsorption strength of N_2 at the saturation pressure point becomes weaker, probably due to the decrease in the specific surface area of the samples, and the all samples are accompanied by H3 hysteresis loops, which suggests the existence of a disordered pore structure in the sample. According to the pore size distribution diagram (Fig. 1B), the pore size of the sample is mainly mesoporous. The corresponding values of the specific surface area (S_{BET}), mesopore volume (V_{meso}) and pore size (d_{pore}) of the measured catalyst are shown in Table S1.† The specific surface area and pore volume of $CAZ_{x/2.0}$-200 decrease to a large extent with increasing etch, while the pore size increases significantly.

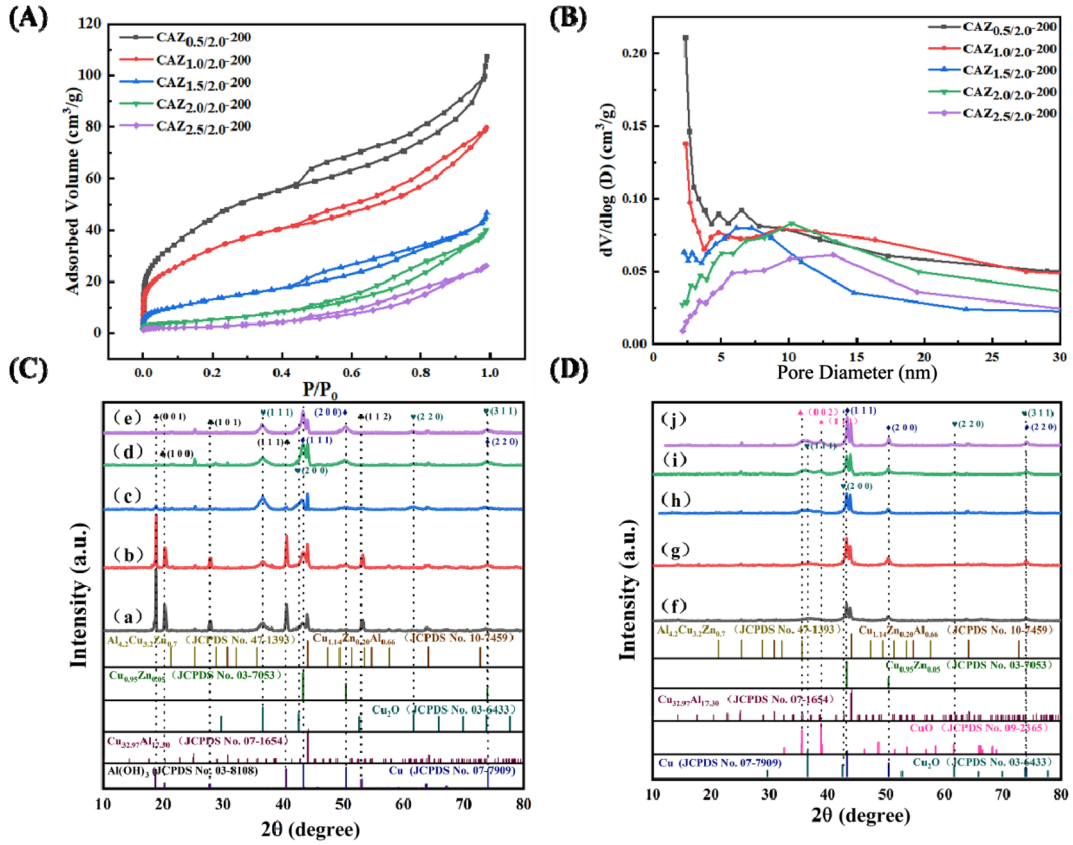

Fig. 1 (A) N_2 adsorption–desorption isotherms; (B) pore size distribution obtained with the $CAZ_{x/2.0}$-200 catalysts. XRD patterns of the catalysts; (C) etched precursor of (a) $CAZ_{0.5/2.0}$, (b) $CAZ_{1.0/2.0}$, (c) $CAZ_{1.5/2.0}$, (d) $CAZ_{2.5/2.0}$ and (e) $CAZ_{2.5/2.0}$; (D) after calcination and reduction of (f) $CAZ_{0.5/2.0}$-200, (g) $CAZ_{1.0/2.0}$-200, (h) $CAZ_{1.5/2.0}$-200, (i) $CAZ_{2.0/2.0}$-200 and (j) $CAZ_{2.5/2.0}$-200.

This phenomenon may be attributed to the structural collapse or pore clogging of the samples with increasing etching degree.

3.1.2 XRD analysis. $CAZ_{x/2.0}$ (x = 0.5, 1.0, 1.5, 2.0, 2.5) precursors were synthesized by alkali etching. The XRD patterns (Fig. 1C) show characteristic diffraction peaks of $Al(OH)_3$ (JCPDS No. 03-8108) at 2θ of 18.7°, 20.3°, 27.8°, 41.3° and 53.0°, corresponding to the (001), (100), (101), (111) and (112) crystal planes.[42] As the degree of etching increases, the diffraction peaks corresponding to the $Al(OH)_3$ crystal planes gradually weaken and disappear. At 43.3°, 50.4° and 74.1°, the diffraction peaks corresponding to the (111), (200) and (220) crystal planes of the Cu (JCPDS No. 07-7909) crystal phase, and at 36.6°, 42.5°, 61.7° and 73.9° show characteristic diffraction peaks of Cu_2O (JCPDS No. 03-6433) belonging to the (111), (200), (220) and (311) crystal planes.[43] Compared with the XRD standard card, some other characteristic peaks are judged to correspond to some alloy crystal phases $Al_{4.2}Cu_{3.2}Zn_{0.7}$ (JCPDS No. 47-1393); $Cu_{1.14}Zn_{0.20}Al_{0.66}$ (JCPDS No. 10-7459); $Cu_{0.95}Zn_{0.05}$ (JCPDS No. 03-7053) and $Cu_{32.97}Al_{17.30}$ (JCPDS No. 07-1654). However, after calcination at 400 °C and reduction at 200 °C, the $Al(OH)_3$ phase disappears and presumably should exist in an amorphous form after dehydration.[23] Cu becomes the main crystalline phase of $CAZ_{x/2.0}$-200 (Fig. 1D), with enhanced characteristic diffraction peaks. Characteristic diffraction peaks corresponding to CuO (JCPDS No. 09-2365)[44] are also observed at 35.5° and 38.8°, corresponding to (002) and (111) crystal plane. The possible reason is that partial stable CuO is formed after calcination, which is difficult to be reduced in the subsequent reduction treatment, and no Al oxide crystal phase is observed. The ICP results show (Table 1) that as the etching degree increases, the content of both Al and Zn decreases to a certain extent during the etching process, thus exposing more Cu sites, which correlates with the results shown in the XRD analysis, as the etching degree enhances, the relative peak intensities of the crystalline phases of the Cu species increase significantly and gradually become the dominant crystalline phase.

3.1.3 SEM and TEM images. The SEM images (Fig. 2A and S1†) show that the $CAZ_{x/2.0}$-200 sample is rough and consists of many irregular micron-sized particles with a pore structure on the surface. The increase in the degree of etching results in an increase in the catalyst pore size and more pronounced particle exposure. EDS analysis of the $CAZ_{1.0/2.0}$-200, $CAZ_{1.5/2.0}$-200 and $CAZ_{2.0/2.0}$-200 samples (Fig. 2D–H and S2†) shows that the Cu species and Zn species are highly uniformly dispersed on the surface of the catalysts, which, in combination with the percentage compositions of all the elements in the EDS elemental profiles (Table S2†), further confirmed the high metal dispersion of Cu and Zn in the defective-site catalysts prepared by the etching method. However, the distribution of Al and O is relatively uneven, this may be due to uneven etching of the Al or

Table 1 Physical properties and catalytic activity of the $CAZ_{x/2.0}$-*M* catalysts

Entry	Catalysts	S_{BET} ($m^2\ g^{-1}$)	Actual atom ratio (Cu/Al/Zn)[d]	FAL conversion[e] (%)	FOL selectivity[e] (%)	FOL yield (%)
1	$CAZ_{0.5/2.0}$-200[a]	168.21	54.85/34.82/4.48	64.22	99.71	64.03
2	$CAZ_{1.0/2.0}$-200[a]	121.13	59.70/24.65/3.96	68.75	99.28	68.26
3	$CAZ_{1.5/2.0}$-200[a]	39.69	74.35/16.63/3.96	98.57	99.69	98.26
4	$CAZ_{2.0/2.0}$-200[a]	16.47	81.61/12.98/3.12	58.22	99.55	57.96
5	$CAZ_{2.5/2.0}$-200[a]	9.17	84.08/12.25/1.97	45.35	99.27	45.92
6	$CAZ_{1.5/2.0}$-200[b]	39.69	74.35/16.63/3.96	0.45	0	0
7	$CAZ_{1.5/2.0}$-200 (R)[c]	—	72.95/15.13/4.02	72.25	96.15	69.47

[a] FAL (1.20 g), catalyst (0.24 g), ethanol (60.0 g), H_2 (1.5 MPa), 80 °C, 5 h. [b] FAL (1.20 g), catalyst (0.24 g), ethanol (60.0 g), N_2 (1.5 MPa), 80 °C, 5 h. [c] FAL (1.20 g), catalyst (0.24 g), ethanol (60.0 g), H_2 (1.5 MPa), 85 °C, 2 h. [d] Actual bulk atom ratio of Cu/Al/Zn was measured by ICP-OES. [e] Experimental error <±5%.

to the formation of some $Al(OH)_3$ when etching Al in a low concentration NaOH solution, and $Al(OH)_3$ may cover the surface of the sample, and the result in turn affects the distribution of Al and O on the surface of the sample,[45] corresponding to the trend shown by XRD that the $Al(OH)_3$ crystal phase in the $CAZ_{x/2.0}$ precursor weakens and disappears with etching.

TEM was used to further determine the structure of the Cu-based skeleton catalyst (Fig. 2B). The HRTEM image (Fig. 2C) of $CAZ_{1.5/2.0}$-200 shows a lattice stripe spacing of 0.208 nm, which belongs to Cu (111).[46] Meanwhile, the catalyst also consists of several components with different lattice spacings, and compared with the XRD standard card, it can be determined that 0.213 nm, 0.302 nm and 0.246 nm correspond to the (200), (110), and (111) crystal planes of Cu_2O, respectively, and that 0.175 nm and 0.212 nm correspond to the (110) and (111) crystal planes of CuO, respectively, indicating that the presence of Cu species with different valence states on the surface of the catalyst. Combined with the SEM analysis, this further confirms the highly dispersed nature of the Cu species. Meanwhile, 0.247 nm corresponds to the (101) crystal plane of ZnO, confirming the presence of ZnO particles.

3.1.4 XPS analysis. The XPS and XAES analysis on synthesized catalysts were carried out to determine the surface composition and oxidation state of element. As shown in Fig. 3A, the binding energy peaks of Cu^{2+} at 933.7 eV and 953.5 eV correspond to Cu $2p_{3/2}$ and Cu $2p_{1/2}$, respectively. The satellite peaks at 941.4 eV, 943.8 eV and 962.1 eV confirm the presence of Cu^{2+}.[47] The two peaks at around 932.4 eV and 952.1 eV are attributed to the Cu $2p_{3/2}$ and Cu $2p_{1/2}$ peaks of Cu^0 or Cu^+, respectively.

It is difficult to distinguish between Cu^0 and Cu^+ based only on the binding energy of Cu 2p,[48] because the kinetic energy difference between XPS distinguishing Cu^0 and Cu^+ is small, which may lead to overlapping results and large analytical errors. Therefore, we used XAES spectroscopy to distinguish between Cu^0 and Cu^+ species (Fig. 3B), and the corresponding kinetic energies of Cu^0, Cu^{2+} and Cu^+ are observed to be 568.6 eV, 573.1 eV, and 576.4 eV, respectively. These results suggest that Cu exists in all three valence states at the catalyst

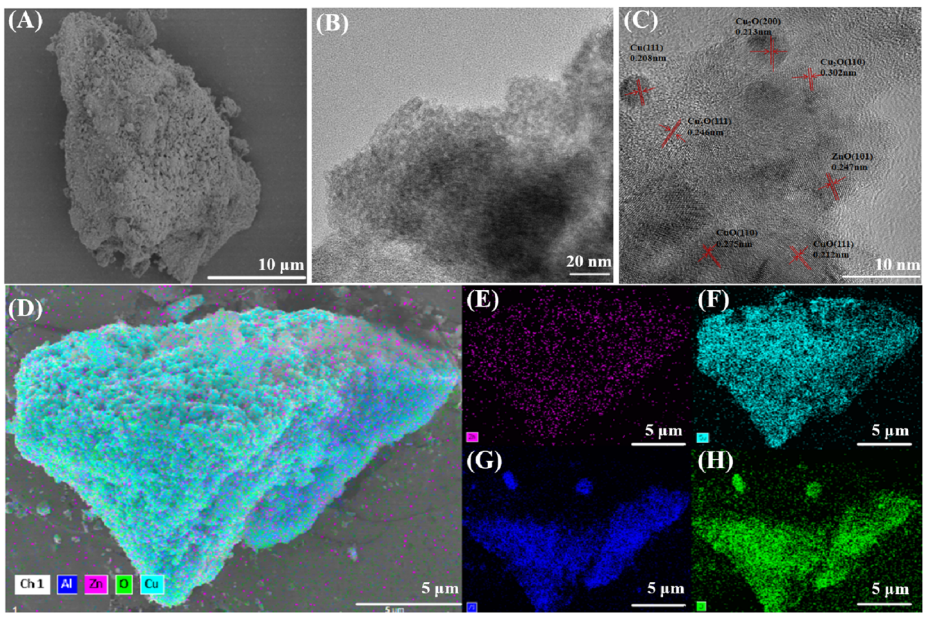

Fig. 2 (A) SEM image; (B) TEM image; (C) HRTEM image; (D–H) EDS elemental mappings of the $CAZ_{1.5/2.0}$-200 catalyst.

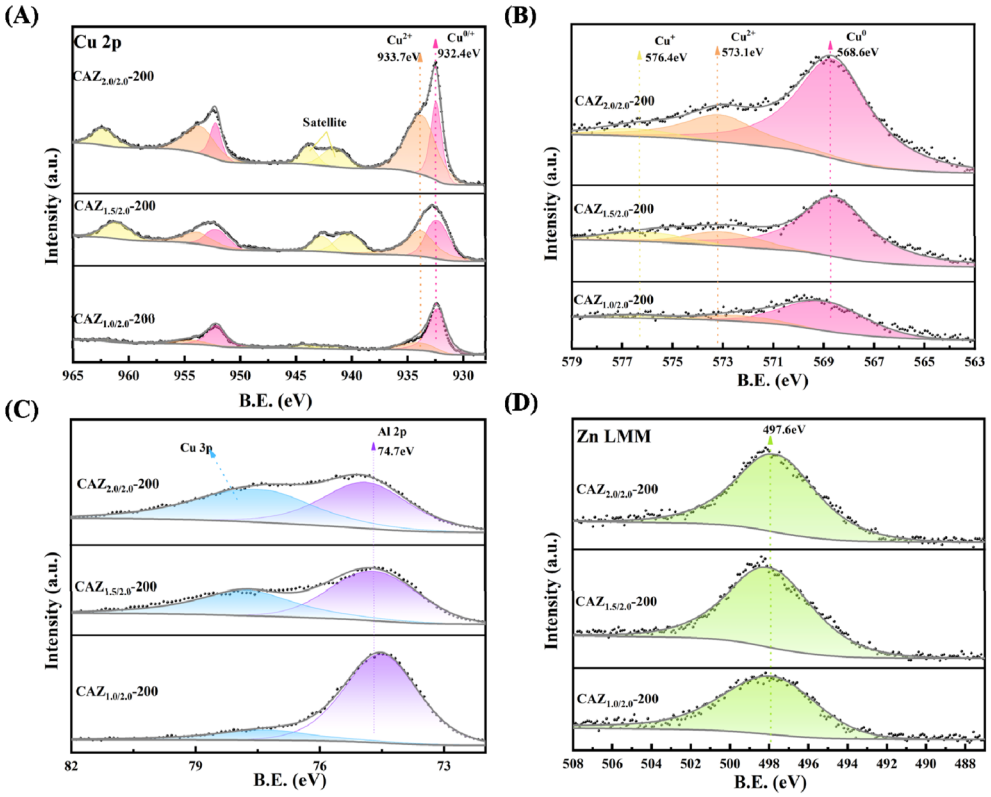

Fig. 3 XPS of these prepared catalysts in (A) Cu 2p spectra, (B) corresponding XAES spectra of Cu LMM, (C) Al 2p spectra, and (D) corresponding XAES spectra of Zn LMM for $CAZ_{1.0/2.0}$-200, $CAZ_{1.5/2.0}$-200 and $CAZ_{2.0/2.0}$-200.

surface.[49] In the Al 2p XPS spectrum of each $CAZ_{x/2.0}$-200 (Fig. 3C), a signal peak at 74.8 eV belongs to Al^{3+} in the $CAZ_{x/2.0}$-200 sample,[50] confirming that Al exists in the form of an oxide. The valence electron state of Zn can be accurately determined by using the XAES spectroscopy. As shown in Fig. 3D, the Zn 2p XAES spectra of each $CAZ_{x/2.0}$-200 sample shows a signal peak belonging to the ZnO species at 989.1 eV, which indicates that Zn exists mainly in the form of oxides on the catalyst surface.

As illustrated in Table S3 and Fig. S3,† the Cu atomic contents in XPS analysis of the $CAZ_{1.0/2.0}$-200, $CAZ_{1.5/2.0}$-200, and $CAZ_{2.0/2.0}$-200 catalysts are 3.92%, 12.19%, and 14.58%, respectively, which are much lower than the corresponding ICP contents (Table 1): 59.70%, 74.35% and 81.61%, respectively, and the Al content is significantly higher, indicating that most of the Cu is stored in the bulk rather than on the surface, the Al content on the surface of the sample is higher than in the bulk, which may be attributed to the fact that the Al in the samples is partially forms into $Al(OH)_3$ and covers on the surface of the samples by the etching process, which is consistent with the results of the XRD and SEM analysis.

3.1.5 NH_3-TPD and Py-IR analysis. NH_3-TPD and Py-IR characterisation show the types and amounts of acidic sites in the catalysts $CAZ_{1.0/2.0}$-200, $CAZ_{1.5/2.0}$-200 and $CAZ_{2.0/2.0}$-200. As shown in Fig. 4A, the desorption peaks in the interval 0–250 °C, 250–450 °C and above 450 °C correspond to the weak acidic sites, medium acidic sites and strong acidic sites of the catalyst, respectively.[51] Sample $CAZ_{1.0/2.0}$-200 has the highest acid content at 1.3902 mmol g^{-1}, with medium and strong acids being the main types. $CAZ_{1.5/2.0}$-200 is mainly medium acidic, with some weak acidic sites and strong acidic sites. The detailed acid amount of the three samples is shown in Table S4,† indicating that the acid amount decreases due to the increase in etching. The weak acidity comes from the desorption of NH_3 weakly adsorbed on the weak Lewis acid sites of the metal center, and the medium acidity comes from the interaction of NH_3 with the Al^{3+} sites in $Al_2O_3 \cdot xH_2O$,[17] while strong acidity comes from the interaction of NH_3 with electron-deficient metal oxides (CuO_x).[52]

The presence of Lewis acid sites on $CAZ_{1.5/2.0}$-200 were confirmed by Py-IR at different adsorption temperatures. As shown in Fig. 4B, the total acid content in the catalyst is measured at 150 °C. When the temperature reaches 200 °C, some weak acids decompose, resulting in a subsequent decrease in the acid content. Most of the medium and weak acids decompose at 350 °C. The bands at 1450 cm^{-1} and 1610 cm^{-1} correspond to the adsorption of pyridine at the Lewis acid sites. The Al_2O_3 can be used as a Lewis acidic center to adsorb the C=O in the FAL,[53] and the CuO can also provide Lewis acidic enhancement to interact with the FAL.[54] The weak peak at 1486 cm^{-1} is a combination of Lewis acid sites and Brønsted acid sites. The small amount of Brønsted acid sites may come from $Al_2O_3 \cdot xH_2O$[55] with different degrees of dehydration and CuO_x.[54] These acidic sites promote the adsorption of FAL on the catalyst. The adsorption of pyridine mainly occurs

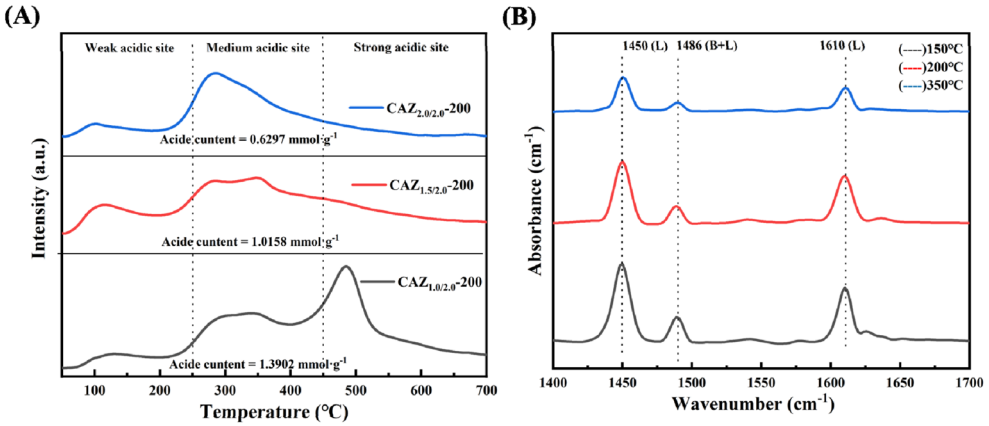

Fig. 4 (A) NH_3-TPD of the catalyst $CAZ_{1.0/2.0}$-200, $CAZ_{1.5/2.0}$-200 and $CAZ_{2.0/2.0}$-200, (B) Py-IR of the catalyst $CAZ_{1.5/2.0}$-200 at different test temperatures.

at Lewis acid sites. The total amount of acid in the catalyst $CAZ_{1.5/2.0}$-200 is shown in Table S5,† which indicates that the catalyst is rich in medium-strength acid sites, and that these acids are mainly present in the form of Lewis acids.

3.1.6 FT-IR spectroscopy. FT-IR analysis provides valuable information about the precursor $CAZ_{x/2.0}$ and $CAZ_{x/2.0}$-200. As shown in Fig. 5A, the important bands in the infrared spectrum include those around 3658 cm^{-1} and 3551 cm^{-1}, which are close to those of belemnite.[56] Significant bands in the IR spectrum of bayerite include those at around 3658 cm^{-1}, 3551 cm^{-1} and 3472 cm^{-1}, which correspond to –OH stretching modes, and there are no significant changes. The infrared bands at 771 cm^{-1} and 532 cm^{-1} are also similar to those of bayerite. The peak at 1637 cm^{-1} originates from free molecular water that is not bonded to Al^{3+}.[57]

The position of the characteristic absorption peak (Fig. 5B) of the sample shifts after calcination and reduction, moving from the typical bayerite 1023 cm^{-1} band to the boehmite 1076 cm^{-1} band, which may be contributed to that after calcination reduction, bayerite is dehydrated and converted to boehmite. Meanwhile, there is a broader typical absorption peak at 3450 cm^{-1}, which may be due to pseudoboehmite.[58] However, it can still be seen that the *in situ* generated $Al_2O_3 \cdot xH_2O$ has a distinct characteristic peak at 738 cm^{-1} and the band at 738 cm^{-1} may be attributed to Al–OH stretching and bending vibrations of boehmite.[59] The broad characteristic peak at around 589 cm^{-1} may also be due to the conversion of bayerite to boehmite.[59]

FT-IR characterisation analysis shows that $Al_2O_3 \cdot xH_2O$ continues to dehydrate in the samples after calcination reduction treatment, verifying the presence of Al_2O_3 in the $CAZ_{x/2.0}$-200 samples, which, combined with XRD analysis, is predominantly present in an amorphous form and supports the origin of the acidic sites in the NH_3-TPD and Py-IR.

3.2 Properties of $CAZ_{1.5/2.0}$-*M* under different reduction conditions

This study used FAL selective hydrogenation technology to evaluate the catalytic activity of $CAZ_{x/2.0}$-*M* catalysts. The activity evaluation was carried out under reaction conditions of 1.5 MPa H_2 pressure, 80 °C, and a reaction time of 5 h. We tested the catalytic performance of $CAZ_{1.5/2.0}$-0, $CAZ_{1.5/2.0}$-100, $CAZ_{1.5/2.0}$-200, and $CAZ_{1.5/2.0}$-300 catalyst powders for FAL selective hydrogenation. As shown in Table 2, the reduced catalyst exhibits significantly higher activity than the unreduced catalyst, which is

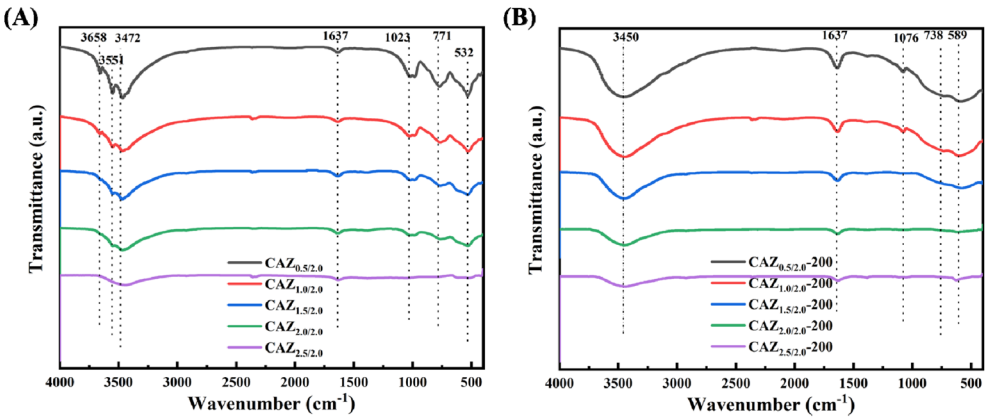

Fig. 5 FT-IR spectra of (A) $CAZ_{x/2.0}$ precursor and (B) $CAZ_{x/2.0}$-200 catalysis.

most likely attributed to the presence of low-valent Cu species (Cu^0 and Cu^+), particularly metallic Cu^0,[60,61] serving as essential active sites for hydrogen adsorption and dissociation. Reduction treatment converts oxidised Cu species (CuO) into low-valent species, which play a crucial role in facilitating hydrogenation reactions by providing active sites for H_2 dissociation and the subsequent interaction with the substrate.[62,63] For catalysts prepared under reducing conditions, this process results in a higher proportion of low-valent Cu species compared to catalysts that are only calcined. As a result, the reduced catalyst exhibits superior catalytic activity due to its enhanced ability to activate hydrogen and promote the reaction.

The influence of different reduction temperatures on the catalytic activity of this reaction is obvious. As the reduction temperature increases, the activity of the catalyst tends to increase and then decrease. In contrast, the catalytic activity of the $CAZ_{1.5/2.0}$-200 sample is significantly improved, with a FAL conversion rate of 98.57% and FOL selectivity of 99.69%. Therefore, so the 200 °C is the optimal reduction temperature, and a series of catalytic characterisations were carried out to explain the changes in activity.

3.2.1 XRD analysis of $CAZ_{1.5/2.0}$-*M*. XRD characterisation was conducted to investigate the effect of reduction temperature on the crystalline structure of Cu species in $CAZ_{1.5/2.0}$-*M* samples prepared under different reduction conditions (Fig. S4†).

The results show that the reduction temperature does not change the crystalline phases of the Cu species, demonstrating the structural stability of the catalyst across different preparation conditions. However, we observed that reduction temperature influences the relative abundance of Cu species with different valence states, which could impact the availability and distribution of active sites crucial for catalytic performance. These findings underscore the significance of carefully controlling reduction parameters to optimise the catalyst's composition and activity.

3.2.2 XPS analysis of $CAZ_{1.5/2.0}$-*M*. Comparing the electronic state analysis of the XPS and XAES surface electrons of the $CAZ_{1.5/2.0}$-100, $CAZ_{1.5/2.0}$-200, and $CAZ_{1.5/2.0}$-300 samples all show similar Cu 2p XPS (Fig. 6A) and Cu 2p XAES (Fig. 6B) spectra. A detailed analysis of the XPS spectra of Cu 2p (Fig. 6A) reveals that, as the reduction temperature increases, the electron density around metallic Cu increases, resulting in a shift of the binding energy to lower values. Theoretically, the complete reduction of Cu species will result in a decrease in the concentration of Cu^{2+} species on the sample surface. Therefore, as shown in Table 2, the proportion of Cu^{2+} in the Cu species in $CAZ_{1.5/2.0}$-*M* decreases and the proportion of low-valent Cu species increases with increasing reduction.

3.2.3 NH_3-TPD and H_2-TPD analysis of $CAZ_{1.5/2.0}$-*M*. The NH_3-TPD characterisation in Fig. 7A shows the types and amounts of acidic sites in the catalysts $CAZ_{1.5/2.0}$-100, $CAZ_{1.5/2.0}$-200 and $CAZ_{1.5/2.0}$-300. The samples are mainly composed of medium acidic sites. Moreover, with the increase of the reduction temperature, the acidity of the samples weakens. For specific acidity, as shown in Table S4.† The reason is that with the increase of the reduction temperature, more CuO is reduced to low-valent Cu species, and the highly dispersed CuO also provides acidic sites,[64] which also enhances the interaction between the catalyst and the substrate FAL.[54]

Analysis of H_2-TPD (Fig. 7B) shows that the main component is chemisorbed (50–200 °C) and dissociated (200–400 °C) hydrogen on the low-temperature peak (<400 °C).[65] The amount of H_2 adsorption capacity is shown in Table S6.† The $CAZ_{1.5/2.0}$-300 sample has the strongest adsorption and dissociation capacity for H_2, while the poor H_2 adsorption capacity of the $CAZ_{1.5/2.0}$-100 is not conducive to the hydrogenation reaction. The adsorption and dissociation capacities of the samples for H_2 increase with the increase of reduction temperature, which may be due to the fact that more CuO is reduced to low-valent Cu with the increase of reduction temperature, and the low-valent Cu species can be used as the sites for adsorption and dissociation of H_2 and thus promote the hydrogenation reaction.[66,67]

The relationship between catalyst activity and the distribution of active components was studied by establishing a structure–activity relationship based on the results of the activity data, NH_3-TPD, H_2-TPD and XPS analysis. The results show that different reduction temperatures control the distribution of Cu species in different valence states, which leads to different catalytic activities in the hydrogenation reaction. The reason for the higher conversion of $CAZ_{1.5/2.0}$-300 than $CAZ_{1.0/2.0}$-100 while ensuring high selectivity (greater than 98.5%) is that $CAZ_{1.5/2.0}$-300 has the strongest ability to adsorb and dissociate H_2, but the reason why the conversion rate of $CAZ_{1.5/2.0}$-200 is significantly the highest is that the optimal ratio of acidic sites and hydrogenation sites has been adjusted, with an appropriate amount of acidic sites and hydrogenation sites. The acidic sites come from the moderate amount of Lewis acid provided by Al_2O_3 and CuO, while the hydrogenation sites come from the adsorption and dissociation of H_2 by low-valent Cu. Together, they synergistically enhance the catalytic activity of FAL for hydrogenation to FOL.

Table 2 Physical properties and catalytic activity of the $CAZ_{1.5/2.0}$-*M* catalysts

Catalysts	Actual atom ratio ($Cu^0/Cu^{2+}/Cu^+$)[b]	(Cu^0 + Cu^+)/(Cu^0 + Cu^+ + Cu^{2+})[b] (%)	Conversion[c] (%)	Selectivity[c] (%)	Yield (%)
$CAZ_{1.5/2.0}$-100[a]	73.48/17.94/8.58	82.06	28.90	98.95	28.60
$CAZ_{1.5/2.0}$-200[a]	76.93/12.27/10.80	87.73	98.57	99.69	98.26
$CAZ_{1.5/2.0}$-300[a]	84.99/10.96/4.05	89.04	76.05	98.88	75.20
$CAZ_{1.5/2.0}$-0[a]	—	—	19.66	98.75	19.41

[a] Reaction conditions: FAL (1.20 g), catalyst (0.24 g), ethanol (60.0 g), 5 h, H_2 (1.5 MPa), 80 °C. [b] Actual bulk atom ratio of $Cu^0/Cu^{2+}/Cu^+$ and (Cu^0 + Cu^+)/(Cu^0 + Cu^+ + Cu^{2+}) were measured by Cu XAES. [c] Experimental error <± 5%.

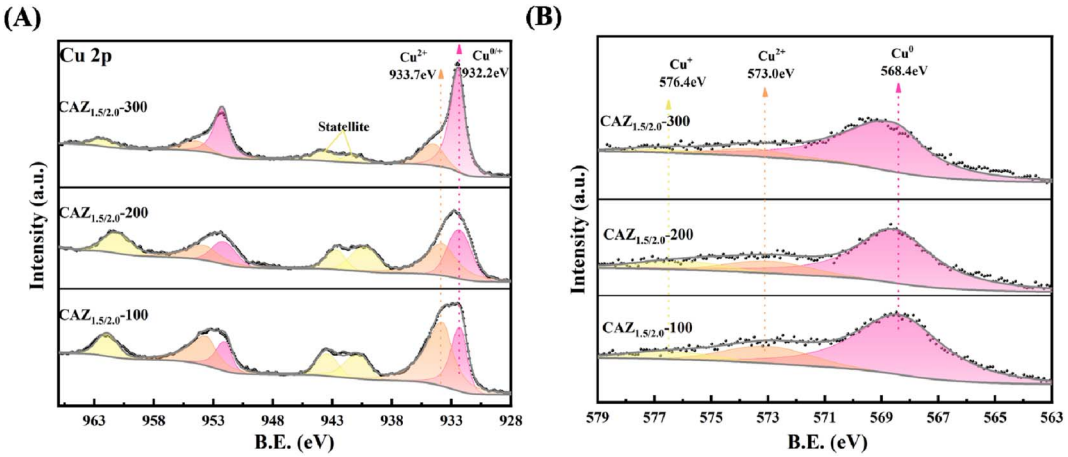

Fig. 6 XPS of the prepared catalysts in (A) Cu 2p spectra, (B) corresponding XAES spectra of Cu LMM.

3.3 Catalytic hydrogenation performance

3.3.1 Effect of catalyst preparation method on catalytic activity. Comparing the catalytic effects of catalysts prepared by the impregnation method (Table 3), under the same reaction conditions, the catalytic activity achieved by the sample with an optimum Cu loading of 35%Cu/Al_2O_3 (18.37% FAL conversion, 93.25% FOL selectivity) is much lower than that of the catalyst etched from the alloy in this study (98.57% FAL conversion, 99.69% FOL selectivity), which may be attributed to the fact that etching the alloys ensures a more homogeneous distribution of Cu species, making dispersed reactive Cu species more accessible, as well as generating interfacial interactions between Cu species and Al_2O_3,[68] which are more prone to synergistic interactions between acidic sites and hydrogenated sites, and further loading of ZnO, catalytic activity and selectivity are further improved (24.18% FAL conversion, 95.47% FOL selectivity). The inferred reason is that the presence of ZnO further enhances the dispersion of Cu species,[69–72] and the Zn and Cu species of the $CAZ_{x/2.0}$-200 catalysts show uniform dispersion in the EDS elemental mappings (Fig. 2D–H and S2†), which enhances the accessibility of the active sites and continues to enhance the catalyst activity. Also, some studies have shown that the presence of ZnO alters the electronic environment around the particles of Cu species, making the catalyst easier to reduce,[22] XPS and XAES spectroscopic analysis of Cu species in the impregnated samples of 35% Cu/Al_2O_3 and 1.33% ZnO/35% Cu/Al_2O_3 (Fig. S5 and Table S7†) show that the presence of further Zn modulated the valence distribution of the Cu making it more readily reducible to lower-valent Cu species. This in turn further improves the catalytic performance. However, compared to the etching catalyst, the catalytic activity of 1.33% ZnO/35% Cu/Al_2O_3 catalytic activity is still limited, the reason is that there may be interfacial interactions between Cu species and Al_2O_3, between ZnO and Al_2O_3,[73] and between ZnO and Cu[74] species in the etched samples, so the catalysts prepared by etching CuAlZn alloys are more likely to synergistically interact with the hydrogenation sites and acidic sites and making the catalyst structure more stable, at the same time, ensure a high degree of dispersion of Cu species, which can increase the accessibility of the active center, less prone to sintering and more catalytic activity. Generation of by-products due to acidic site-catalysed polymerisation reaction, generating humin, a polymerisation reactant produced in the FAL.[75]

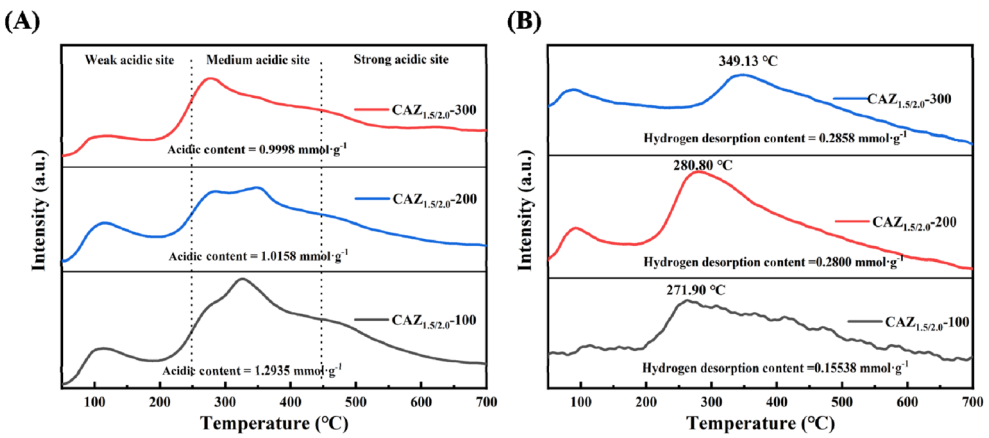

Fig. 7 (A) NH_3-TPD of the catalyst $CAZ_{1.0/2.0}$-200, $CAZ_{1.5/2.0}$-200 and $CAZ_{2.0/2.0}$-200, (B) H_2-TPD of the catalyst $CAZ_{1.0/2.0}$-200, $CAZ_{1.5/2.0}$-200 and $CAZ_{2.0/2.0}$-200.

Table 3 Comparison of catalytic activity of catalysts obtained by different preparation methods

Catalysts	Conversion[b] (%)	Selectivity[b] (%)	Yield (%)
$CAZ_{1.5/2.0}$-200[a]	98.57	99.69	98.26
25% Cu/Al_2O_3[a]	6.07	88.14	5.35
35% Cu/Al_2O_3[a]	18.37	93.25	17.13
45% Cu/Al_2O_3[a]	14.96	97.74	14.62
1.33% ZnO/35% Cu/Al_2O_3[a]	24.18	95.47	23.08

[a] Reaction conditions: FAL (1.20 g), catalyst (0.24 g), ethanol (60.0 g), 5 h, H_2 (1.5 MPa), 80 °C. [b] Experimental error <± 5%.

3.3.2 Catalytic activity of $CAZ_{x/2.0}$-200. The effect of different degrees of etching on the catalytic activity of the $CAZ_{x/2.0}$-200 catalyst was investigated by using the model reaction of FAL hydrogenation to FOL, and the activity evaluation was carried out under the reaction conditions of 1.5 MPa H_2, 80 °C, 5 h. As shown in Table 1, with the increase of etching degree, the catalysts all show high selectivity (>99.0%) and the catalytic activity tends to increase and then decrease under the same conditions of other preparation methods. Among them, $CAZ_{1.5/2.0}$-200 shows the best catalytic activity with 98.57% FAL conversion. Further bases on the results of ICP analysis, the etching during the catalyst preparation leads to different degrees of leaching of both Al and Zn, which indicates that the relative content of Cu/Al/Zn reaches a certain equilibrium to be conducive to the optimal performance of the catalyst activity.

3.3.3 Effect of reaction conditions on the catalytic performance of $CAZ_{1.5/2.0}$-200. In addition, the effect of different reaction conditions (H_2 pressure, reaction time and temperature) on the catalytic performance of the $CAZ_{1.5/2.0}$-200 catalyst with the best catalytic performance was investigated. As can be shown in Fig. 8A–C, from 70 °C to 85 °C, the conversion of FAL gradually increases with the increase of temperature, while the selectivity of FOL remains at a high level but shows a slight decrease, the reason for the production of by-products may be the formation of humin with the increase of reaction conditions. The trends of the effects of reaction time (1–5 h) and H_2 pressure (0.5–1.5 MPa) on catalytic activity at the fixed optimum reaction temperature of 85 °C are similar, indicating that longer reaction time and higher H_2 pressures have a beneficial effect on FAL conversion. In addition, comparative experiments

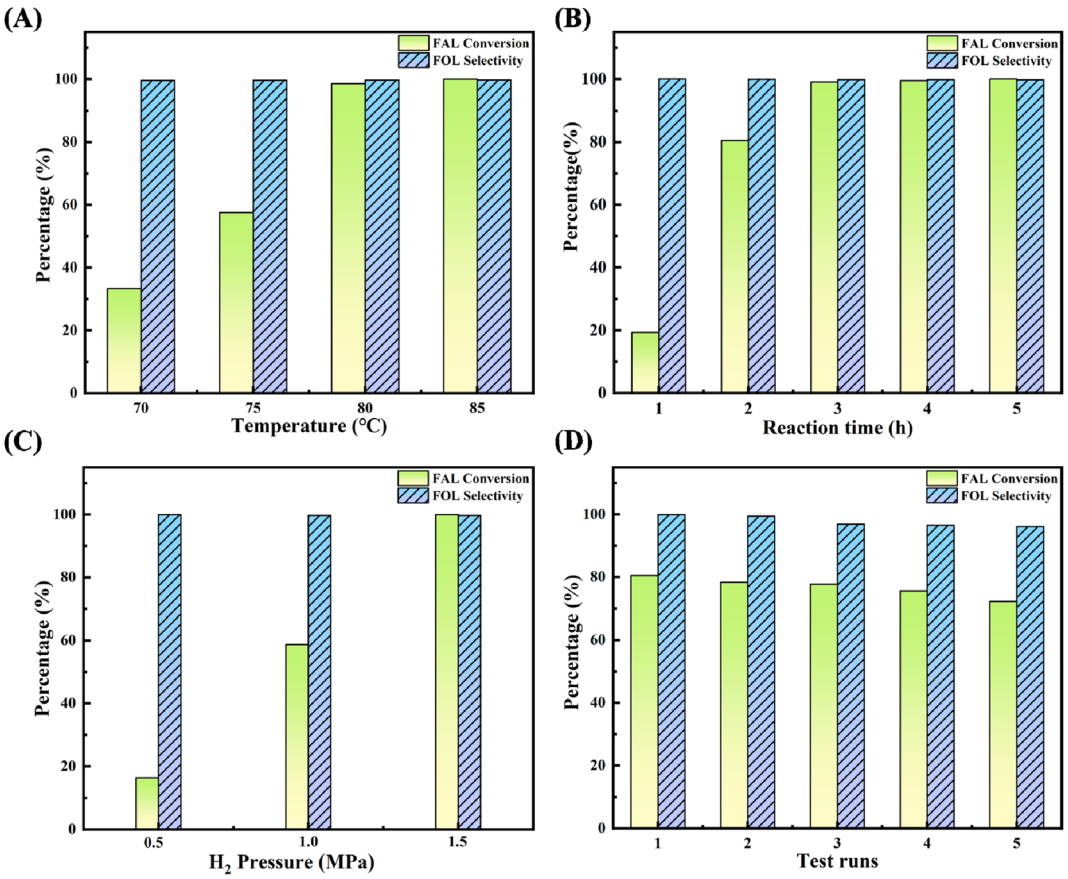

Fig. 8 The effect of reaction conditions on activity and reusability of the $CAZ_{1.5/2.0}$-200 catalyst (reaction conditions: FAL (1.20 g), catalyst (0.24 g), ethanol (60.0 g), (A) 1.5 MPa H_2, 5 h; (B) 85 °C, 1.5 MPa H_2; (C) 85 °C, 4 h; (D) 85 °C, 1.5 MPa H_2, 2 h).

Table 4 Comparison of FAL conversion to FOL catalyzed by various heterogeneous catalysts

Catalysts	Reaction conditions	FAL conversion (%)	FOL selectivity (%)	m_{FAL} (g)/ m_{Cat} (g)	Productivity (mol FOL g (cat)$^{-1}$ h^{-1})
C@Ni_3P[25]	140 °C, 1.4 MPa H_2, 4 h	97	96.3	5.0	0.01215
$Cu_2Ni_1AlO_y$[23]	120 °C, 1.6 MPa H_2, 1.5 h	98	99	5.0	0.03366
Cu/MgO[76]	110 °C, 2 MPa H_2, 80 min	99.9	99.9	1.152	0.00897
NiCoCuZnFe/C-800 (ref. 77)	90 °C, 3 MPa H_2, 9 h	87.3	100	6	0.00606
Fh-$Al_{0.67}$ (ref. 78)	150 °C, 1 MPa N_2, 5 h	100	100	1.92	0.00340
Ru/ZP-A[79]	90 °C, 1.25 MPa H_2, 7 h	62	97	2.07	0.00185
Ni–Mg–Al[80]	140 °C, 3 h	98.5	98.98	2.304	0.00780
Fe_3O_4@C[81]	200 °C, 2 MPa N_2, 4 h	93.6	98.9	3.84	0.00925
15Cu–15Ni/MCM-41 (ref. 82)	160 °C, 4 h	94.5	99	1.92	0.00467
2% Ni–5% Cu/SiO_2 (ref. 83)	100 °C, 2 MPa H_2, 2 h	94	64	0.290	0.00091
$CAZ_{1.5/2}$-200 (this work)	85 °C, 1.5 MPa H_2, 3 h	>99.0	>99.0	5	0.01700

(Table 1) on $CAZ_{1.5/2}$-200 catalyst with N_2 instead of H_2 under the same reaction conditions (1.5 MPa, 85 °C, 5 h) did not yield any activity for generating FOL. This confirms that molecular H_2 is the only hydrogen donor for the preparation of FOL by the FAL hydrogenation reaction. In summary, the $CAZ_{1.5/2}$-200 catalyst exhibits good catalytic activity under the conditions of 1.5 MPa H_2, 85 °C, and a reaction time of 3 h, with a FAL conversion rate of 99.10% and a FOL selectivity of 99.84%.

3.3.4 Reusability of $CAZ_{1.5/2}$-200. The reusability of the $CAZ_{1.5/2}$-200 optimal catalyst was investigated under the

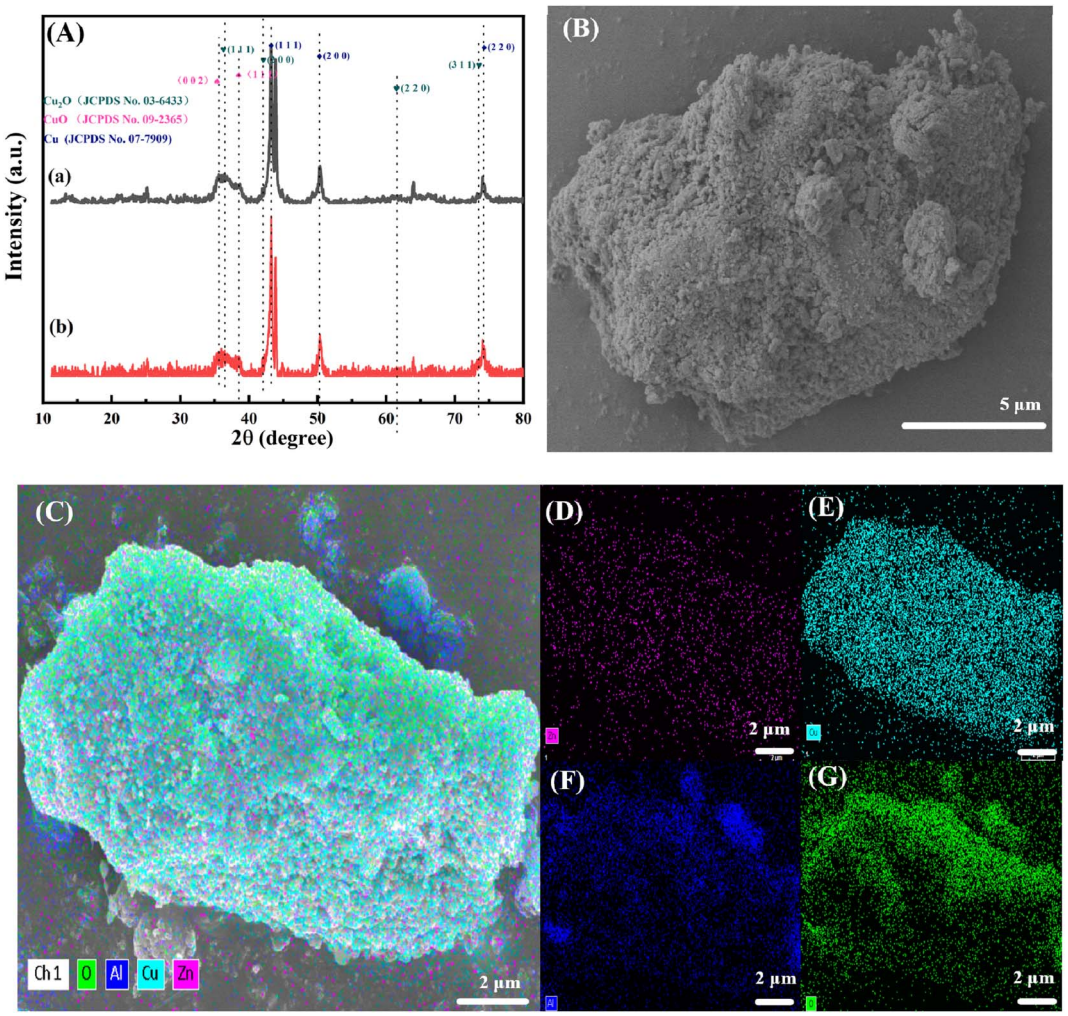

Fig. 9 (A) XRD patterns of catalysts: the fresh catalyst $CAZ_{1.5/2.0}$-200 (a) and the recovered catalyst $CAZ_{1.5/2.0}$-200 (R) (b); (B) SEM image of the recovered catalyst $CAZ_{1.5/2.0}$-200 (R); (C–G) EDS elemental mappings of the recovered catalyst $CAZ_{1.5/2.0}$-200 (R).

reaction conditions of H_2 pressure of 1.5 MPa, reaction temperature of 85 °C, and reaction time of 2 h. As shown in Fig. 8D, the FOL yield of the $CAZ_{1.5/2}$-200 catalyst in the fourth cycle is still above 75%, indicating that the $CAZ_{1.5/2}$-200 catalyst has good reusability. Table 4 summarizes the catalytic performances of other hydrogenation catalysts for FAL to FOL reported in the literature. In comparison, our $CAZ_{1.5/2}$-200 can achieve better reactivity under milder reaction conditions, with a FAL conversion of >99.0% and a FOL selectivity of >99.0%. Therefore, our work has certain advantages for the catalytic selective hydrogenation of FAL to FOL under mild reaction conditions.

3.4 Characterisation of the recovered catalyst

In order to analyse the mechanism of catalyst deactivation, the recovered catalyst (after five reaction processes and calcination then reduction, named $CAZ_{1.5/2.0}$-200 (R)) was further studied. XRD analysis of the recovered catalyst (Fig. 9A) shows that the intensities of the corresponding crystalline phase peaks of CuO, Cu_2O and alloys decrease, and the relative intensity of the Cu crystalline phase increases, indicating that the recovered catalyst is more readily reducible to low-valent metals. Compared with fresh catalyst, ICP analysis of the recovered catalyst (Table 1) shows that Cu ($CAZ_{1.5/2.0}$-200 (R): 72.95%; $CAZ_{1.5/2.0}$-200: 74.35%) and Al ($CAZ_{1.5/2.0}$-200 (R): 15.13%; $CAZ_{1.5/2.0}$-200:16.63%) have slightly leach. Comparing the morphology (Fig. 9B) and mapping characterisation results (Fig. 9C–G) of fresh and recovered catalyst, it is relatively consistent. Therefore, the recovered catalyst can be reused well, but the slight decrease in activity can be attributed to the reduction of low-valent Cu species and the slight leaching of Cu and Al.

4. Conclusions

In summary, this study utilised the etching method to synthesise a composite metal oxide catalyst for the selective hydrogenation of FAL to FOL. Among the catalysts tested, $CAZ_{1.5/2}$-200 demonstrated the highest catalytic performance, achieving over 99.0% FAL conversion and 99.0% FOL selectivity under mild conditions of 1.5 MPa H_2 at 85 °C for 3 h. This exceptional activity is primarily attributed to the synergistic effect between low-valent Cu species, which act as active sites for H_2 adsorption and dissociation, and Lewis acid sites provided by Al_2O_3 and CuO, which enhance FAL adsorption. The interaction between ZnO and Cu modifies the electronic environment around the Cu species, facilitating their reduction to low-valent states and improving Cu dispersion. Compared to traditional impregnation methods, the alloy etching approach strengthens interfacial interactions between species, promoting a stronger synergistic effect between acidic and hydrogenation sites. This leads to a more stable catalyst structure with enhanced activity and reusability. Furthermore, the simple and cost-effective preparation process offers a promising strategy for the rational design of efficient hydrogenation catalysts for FAL to FOL conversion under mild reaction conditions.

Data availability

Characterisation and evaluations are displayed in the manuscript, and other characterisation analysis figures, tables and the specific experimental data supporting this article have been included as part of the ESI.†

Author contributions

Junqi Zhang: conceptualization, methodology, formal analysis, investigation, writing – original draft. Yongwang Li: conceptualization, methodology, supervision. Zhiwei Zhang: conceptualization, supervision, writing – review & editing. Zheng Wang: data curation, supervision. Jiaxing Zhang: conceptualization, methodology, supervision. Shuai Liu: validation, data curation, formal analysis. Yang Qin: validation, data curation. Bingxin Zhu: validation, data curation. Tongxue Zhang: validation, data curation. Hongyu Wang: validation, data curation. Fumin Wang: conceptualization, methodology, supervision. Xubin Zhang: validation, data curation, formal analysis.

Conflicts of interest

There are no conflicts to declare.

Acknowledgements

This work was supported by the National Natural Science Foundation of China (Grant No. 22211540711, 22479109), the Natural Science Foundation of Shandong Province (Grant No. ZR2023ZD22), and the Major R&D Program of Shandong Province (Grant No. 2023CXGC010601).

References

1 W. Gao, S. Liang, R. Wang, Q. Jiang, Y. Zhang, Q. Zheng, B. Xie, C. Y. Toe, X. Zhu, J. Wang, L. Huang, Y. Gao, Z. Wang, C. Jo, Q. Wang, L. Wang, Y. Liu, B. Louis, J. Scott, A.-C. Roger, R. Amal, H. He and S.-E. Park, Industrial carbon dioxide capture and utilization: state of the art and future challenges, *Chem. Soc. Rev.*, 2020, **49**, 8584–8686.

2 Y. Yang, Z. Ren, S. Zhou and M. Wei, Perspectives on multifunctional catalysts derived from layered double hydroxides toward upgrading reactions of biomass resources, *ACS Catal.*, 2021, **11**, 6440–6454.

3 L. Lei, Y. Wang, Z. Zhang, J. An and F. Wang, Transformations of biomass, its derivatives, and downstream chemicals over ceria catalysts, *ACS Catal.*, 2020, **10**, 8788–8814.

4 P. Zhou, Y. Chen, P. Luan, X. Zhang, Z. Yuan, S. X. Guo, Q. Gu, B. Johannessen, M. Mollah, A. L. Chaffee, D. R. Turner and J. Zhang, Selective electrochemical hydrogenation of furfural to 2-methylfuran over a single atom Cu catalyst under mild pH conditions, *Green Chem.*, 2021, **23**, 3028–3038.

5 J. P. Lange, E. Van Der Heide, J. van Buijtenen and R. Price, Furfural-a promising platform for lignocellulosic biofuels, *ChemSusChem*, 2012, **5**(1), 150–166.

6 P. Jia, X. C. Lan, X. D. Li and T. Wang, Highly selective hydrogenation of furfural to cyclopentanone over a NiFe bimetallic catalyst in a methanol/water solution with a solvent effect, *ACS Sustain. Chem. Eng.*, 2019, **7**, 15221–15229.

7 K. Yan, G. Wu, T. Lafleur and C. Jarvis, Production, properties and catalytic hydrogenation of furfural to fuel additives and value-added chemicals, *Renewable Sustainable Energy Rev.*, 2014, **38**, 663–676.

8 V. Pace, P. Hoyos, L. Castoldi, P. Domínguez de María and A. R. Alcántara, 2-Methyltetrahydrofuran (2-MeTHF): a biomass-derived solvent with broad application in organic chemistry, *ChemSusChem*, 2012, **5**(8), 1369–1379.

9 Z. Wang, X. Wang, C. Zhang, Y. Yang, L. Zhou, H. Cheng and F. Zhao, Selective hydrogenolysis of tetrahydrofurfuryl alcohol to 1,5-pentanediol over PrO_x promoted Ni catalysts, *Catal. Today*, 2022, **402**, 79–87.

10 X. Fu, X. Ren, J. Shen, Y. Jiang, Y. Wang, Y. Orooji, W. Xu and J. Liang, Synergistic catalytic hydrogenation of furfural to 1,2-pentanediol and 1,5-pentanediol with LDO derived from CuMgAl hydrotalcite, *Mol. Catal.*, 2021, **499**, 111298.

11 J. Zhang, Y. Liu, Z. Jia, S. Liu, L. Li, Q. Wu and C. Xu, Selective hydrogenation of furfural to furfuryl alcohol over copper-cobalt bimetallic catalyst, *Chem. Eng. J.*, 2024, **490**, 151677.

12 Y. Shi, T. Wu, Z. Wang, C. Liu, J. Bi and L. Wu, Photocatalytic precise hydrogenation of furfural over ultrathin Pt/NiMg-MOF-74 nanosheets: Synergistic effect of surface optimized Ni^{II} sites and Pt clusters, *Appl. Surf. Sci.*, 2023, **616**, 156553.

13 Y. Ren, Y. Yang, L. Chen, L. Wang, Y. Shi, P. Yin, W. Wang, M. Shao, X. Zhang and M. Wei, Synergetic effect of Cu^0-Cu^+ derived from layered double hydroxides toward catalytic transfer hydrogenation reaction, *Appl. Catal. B-Environ.*, 2022, **314**, 121515.

14 R. Mariscal, P. Maireles-Torres, M. Ojeda, I. Sadaba and M. L. Granados, Furfural: a renewable and versatile platform molecule for the synthesis of chemicals and fuels, *Energy Environ. Sci.*, 2016, **9**(4), 1144–1189.

15 Z. Zhao, R. Bababrik, W. Xue, Y. Li, N. M. Briggs, D. T. Nguyen, U. Nguyen, S. P. Crossley, S. Wang, B. Wang and D. E. Resasco, Solvent-mediated charge separation drives alternative hydrogenation path of furanics in liquid water, *Nat. Catal.*, 2019, **2**(5), 431–436.

16 Y. Dai, X. Gao, X. Chu, C. Jiang, Y. Yao, Z. Guo, C. Zhou, C. Wang, H. Wang and Y. Yang, On the role of water in selective hydrogenation of cinnamaldehyde to cinnamyl alcohol on PtFe catalysts, *J. Catal.*, 2018, **364**, 192–203.

17 Q. Shen, Y. Li, F. Wang, X. Zhang, Z. W. Zhang, Z. L. Zhang, Y. Yang, C. Bing, X. Fan, J. Zhang and X. He, Controlled targeted conversion of furfural to 1,5-pentanediol or 2-methylfuran over Ni/$CoAlO_x$ catalyst, *Mol. Catal.*, 2024, **556**, 113919.

18 X. Li, P. Jia and T. Wang, Furfural: A promising platform compound for sustainable production of C_4 and C_5 chemicals, *ACS Catal.*, 2016, **6**(11), 7621–7640.

19 C. P. Jiménez-Gómez, J. A. Cecilia, D. Durán-Martín, R. Moreno-Tost, J. Santamaría-González, J. Mérida-Robles, R. Mariscal and P. Maireles-Torres, Gas- phase hydrogenation of furfural to furfuryl alcohol over Cu/ZnO catalysts, *J. Catal.*, 2016, **336**, 107–115.

20 K. Fulajtárova, T. Soták, M. Hronec, I. Vávra, E. Dobročka and M. Omastová, Aqueous phase hydrogenation of furfural to furfuryl alcohol over Pd-Cu catalysts, *Appl. Catal., A*, 2015, **502**, 78–85.

21 M. J. Taylor, S. K. Beaumont, M. J. Islam, S. Tsatsos, C. A. M. Parlett, M. A. Issacs and G. Kyriakou, Atom efficient PtCu bimetallic catalysts and ultra dilute alloys for the selective hydrogenation of furfural, *Appl. Catal., B*, 2021, **284**, 119737.

22 G. R. Bertolini, C. P. Jiménez-Gómez, J. A. Cecilia and P. Maireles-Torres, Gas-phase hydrogenation of furfural to furfuryl alcohol over Cu-ZnO-Al_2O_3 catalysts prepared from layered double hydroxides, *Catalysts*, 2020, **10**(5), 486.

23 L. Luo, F. L. Yuan, F. Zaera and Y. J. Zhu, Catalytic hydrogenation of furfural to furfuryl alcohol on hydrotalcite-derived $Cu_xNi_{3-x}AlO_y$ mixed-metal oxides, *J. Catal.*, 2021, **404**, 420–429.

24 M. Kalong, P. Hongmanorom, S. Ratchahat, W. Koo-amornpattana, K. Faungnawakij, S. Assabumrungrat, A. Srifa and S. Kawi, Hydrogen-free hydrogenation of furfural to furfuryl alcohol and 2-methylfuran over Ni and Co-promoted Cu/γ-Al_2O_3 catalysts, *Fuel Process. Technol.*, 2021, **214**, 106721.

25 Y. Tian, Y. Z. Wang, H. Y. Zhang, L. F. Xiao and W. Wu, Novel C@Ni_3P nanoparticles for highly selective hydrogenation of furfural to furfuryl alcohol, *Catal. Lett.*, 2022, **152**(3), 883–894.

26 S. H. Liu, N. Govindarajan and K. Chan, Understanding activity trends in furfural hydrogenation on transition metal surfaces, *ACS Catal.*, 2022, **12**, 12902–12910.

27 M. J. Islam, M. G. Mesa, A. Osatiashtiani, J. C. Manayil, M. A. Isaacs, M. J. Taylor and S. T. G. Kyriakou, PdCu single atom alloys supported on alumina for the selective hydrogenation of furfural, *Appl. Catal. B-Environ.*, 2021, **299**, 120652.

28 M. J. Islam, M. G. Mesa, A. Osatiashtiani, M. J. Taylor, J. C. Manayil, C. M. Parlett and G. Kyriakou, The effect of metal precursor on copper phase dispersion and nanoparticle formation for the catalytic transformations of furfural, *Appl. Catal. B-Environ.*, 2020, **273**, 119062.

29 W. B. Gong, C. Chen, Y. Zhang, H. Zhou, H. Wang, H. Zhang, Y. Zhang, G. Z. Wang and H. J. Zhao, Efficient synthesis of furfuryl alcohol from H_2-hydrogenation/transfer hydrogenation of furfural using sulfonate group modified Cu catalyst, *ACS Sustain. Chem. Eng.*, 2017, **5**, 2172–2180.

30 J. Lee, J. H. Seo, C. Nguyen-Huy, E. Yang, J. G. Lee, H. Lee, E. J. Jang, J. H. Kwak, J. H. Lee, H. Lee and K. An, Cu_2O(100) surface as an active site for catalytic furfural hydrogenation, *Appl. Catal. B-Environ.*, 2021, **282**, 119576.

31 X. Q. Wang, Q. Chen, Y. J. Zhou, H. M. Li, J. W. Fu and M. Liu, Cu-based bimetallic catalysts for CO_2 reduction reaction, *Adv. Energy Mater.*, 2022, **1**(3), 100023.

32 D. Sharma, J. Suriyaprakash, A. Dogra, S. Alijani, A. Villa and N. Gupta, Versatile carbon supported mono and bimetallic nanocomposites: synthesis, characterization and their potential application for furfural reduction, *Mater. Today Chem.*, 2020, **17**, 100319.

33 L. Ma and M. S. Wainwright, Development of skeletal copper–chromia catalysts: I. Structure and activity promotion of chromia on skeletal copper catalysts for methanol synthesis, *Appl. Catal., A*, 1999, **187**(1), 89–98.

34 X. Liu, D. Sun, Y. Ji, S. Zu, Y. Pei, S. Yan, M. Qiao, X. Zhang and B. Zong, Effect of NaOH concentration on rapidly quenched Cu-Al alloy-derived Cu catalyst for CO_2 hydrogenation to CH_3OH, *Catalysts*, 2024, **14**(6), 391.

35 R. Yao, Y. Li, X. Zhang, Y. Zhao, Y. Wang, X. Lang, Q. Jiang, H. Tan and Y. Li, Self-supported nanoporous CuNiAl alloy as highly efficient electrocatalyst for nitrobenzene hydrogenation to aniline, *Chem. Eng. J.*, 2023, **471**, 144487.

36 L. Geng, Z. Lin, Z. Li, S. An, X. Zhang, Z. Liu, D. S. Zhang, Y. Z. Zhang, S. Gao and H. Han, Facile synthesis of holey lamellar CuO *via* ultrasonic chemical etching toward highly efficient hydrogenation of 4-nitrophenol under mild conditions, *J. Solid State Chem.*, 2020, **292**(1), 121698.

37 H. Hu, F. Xie, Y. Pei, M. Qiao, S. Yan, H. He, K. Fan, H. Li, B. Zong and X. Zhang, Skeletal Ni catalysts prepared from Ni-Al alloys rapidly quenched at different rates: Texture, structure and catalytic performance in chemoselective hydrogenation of 2-ethylanthraquinone, *J. Catal.*, 2006, **237**(1), 143–151.

38 Z. Sun, Z. H. Zhang, T. Q. Yuan, X. Ren and Z. Rong, Raney Ni as a versatile catalyst for biomass conversion, *ACS Catal.*, 2021, **11**, 10508–10536.

39 Y. Jiang, Q. Chang, L. Guan, B. Teng, C. Xu, Y. Zhang, X. Li, Q. Sheng, Y. Yao, S. Lu and Y. Qin, Efficient C = O bond hydrogenation of cinnamaldehyde over Pt-Cu alloy frame: Insight into the morphology and Pt species state, *Chem. Eng. J.*, 2023, **477**, 146854.

40 T. Zheng, Y. Zhu, R. Ma, L. Bai, H. Yu, S. Zhao, Y. He, Y. Liu and D. Li, Construction of Enriched Metal Vacancies to Enhance Catalytic Behavior for Selective Hydrogenation Over Au-Cu Nanoalloys, *Ind. Eng. Chem. Res.*, 2024, **63**, 2717–2725.

41 Y. B. Huang, J. L. Zhang, X. Zhang, X. Luan, H. Z. Chen, B. Hu, L. Zhao, Y. L. Wu and Q. Lu, Catalytic depolymerization of lignin *via* transfer hydrogenation strategy over skeletal CuZnAl catalyst, *Fuel Process. Technol.*, 2022, **237**, 107448.

42 B. S. Vasile, G. Dobra, S. Iliev, L. Cotet, I. A. Neacsu, V. A. Surdu, A. I. Nicoara, A. Boiangiu and L. Filipescu, Thermally activated Al $(OH)_3$ part II-effect of different thermal treatments, *Ceram.*, 2021, **4**(4), 564–575.

43 Z. W. Guo, F. Zhou, H. Wang, X. H. Liu, G. Y. Xu, Y. Zhang and Y. Fu, Highly selective conversion of natural oil to alcohols or alkanes over a Pd stabilized CuZnAl catalyst under mild conditions, *Green Chem.*, 2019, **21**, 5046–5052.

44 K. K. Miao, X. L. Luo, W. Wang, J. L. Guo, S. F. Guo, F. J. Cao, Y. Q. Hu, P. M. Chang and G. D. Feng, One-step synthesis of Cu-SBA-15 under neutral condition and its oxidation catalytic performance, *Microporous Mesoporous Mater.*, 2019, **289**, 109640.

45 Y. Huang, D. K. Sarkar and X. G. Chen, Superhydrophobic aluminum alloy surfaces prepared by chemical etching process and their corrosion resistance properties, *Appl. Surf. Sci.*, 2015, **356**, 1012–1024.

46 D. D. Li, F. Xu, X. Tang, S. Dai, T. C. Pu, X. L. Liu, P. F. Tian, F. Z. Xuan, Z. Xu, I. E. Wachs and M. H. Zhu, Induced activation of the commercial $Cu/ZnO/Al_2O_3$ catalyst for the steam reforming of methanol, *Nat. Catal.*, 2022, **5**(2), 99–108.

47 F. J. Lan, H. L. Zhang, C. Y. Zhao, Y. Shu, Q. X. Guan and W. Li, Copper clusters encapsulated in carbonaceous mesoporous silica nanospheres for the valorization of biomass-derived molecules, *ACS Catal.*, 2022, **12**(9), 5711–5725.

48 J. Luo, Y. Cheng, H. Niu, T. Wang and C. Liang, Efficient Cu/FeO_x catalyst with developed structure for catalytic transfer hydrogenation of furfural, *J. Catal.*, 2022, **413**, 575–587.

49 J. Zhang, Y. M. Liu, Z. Jia, S. Yu, S. Liu, L. Li, Q. Wu, H. Yu, Y. X. Liu, X. Jiang, Y. Liu and C. Xu, Selective hydrogenation of furfural to furfuryl alcohol over copper-cobalt bimetallic catalyst, *Chem. Eng. J.*, 2024, **490**, 151677.

50 Q. Liu, H. Qin, J. A. Boscoboinik and G. Zhou, Comparative study of the oxidation of NiAl (100) by molecular oxygen and water vapor using ambient-pressure X-ray photoelectron spectroscopy, *Langmuir*, 2016, **32**(44), 11414–11421.

51 L. Hu, M. Yang, N. Xu, J. Xu, S. Zhou, X. Chu and Y. Zhao, Selective transformation of biomass-derived 5-hydroxymethylfurfural into 2,5-dihydroxymethylfuran *via* catalytic transfer hydrogenation over magnetic zirconium hydroxides, *Korean J. Chem. Eng.*, 2018, **35**, 99–109.

52 M. Tu, D. T. Li, J. Y. Shen and Y. Chen, Microcalorimetric studies of surface acidity and basicity of metal oxides, *Chem. J. Chin. Univ.*, 1998, **19**, 946–949.

53 S. Rajagopal, J. A. Marzari and R. Miranda, Silica-alumina-supported Mo oxide catalysts: Genesis and demise of Brønsted-Lewis acidity, *J. Catal.*, 1995, **151**(1), 192–203.

54 J. Zhang, C. Li, S. Hu, J. Gu, H. Yuan and Y. Chen, Mechanistic insights into copper oxides catalyzed bio-based furfural hydrogenation using methanol as in situ hydrogen donor, *Renewable Energy*, 2022, **200**, 88–97.

55 S. Srivastava, G. C. Jadeja and J. Parikh, Synergism studies on alumina-supported copper-nickel catalysts towards furfural and 5-hydroxymethylfurfural hydrogenation, *J. Mol. Catal. A:Chem.*, 2017, **426**, 244–256.

56 K. A. Rodgers, M. R. Gregory and R. P. Cooney, Bayerite, $Al(OH)_3$, from Raoul Island, Kermadec Group, South Pacific, *Clay Miner.*, 1989, **24**(3), 531–538.

57 G. Y. Wei, J. K. Qu, Y. D. Zheng, Q. I. Tao, G. U. O. Qiang, B. B. Han and H. X. Zhao, Crystallization behaviors of bayerite from sodium chromate alkali solutions, *Trans. Nonferrous Met. Soc. China*, 2014, **24**(10), 3356–3365.

58 S. Musić, D. Dragčević, S. Popović and N. Vdović, Microstructural properties of boehmite formed under hydrothermal conditions, *Mater. Sci. Eng., B*, 1998, **52**(2–3), 145–153.

59 S. Musić, Đ. Dragčević, S. Popović and N. Vdović, Chemical and microstructural properties of Al-oxide phases obtained from $AlCl_3$ solutions in alkaline medium, *Mater. Chem. Phys.*, 1999, **59**(1), 12–19.

60 J. Zhang, X. Yang, Z. Jia, Q. Han, S. Yu, S. Liu, L. Li, Q. Wu, H. Yu, Y. X. Liu and Y. Liu, Bi-functional active sites Cu/MgO-La_2O_3 catalysts the selective hydrogenation of furfural to furfuryl alcohol, *Chem. Eng. J.*, 2024, **500**, 157400.

61 J. Tan, J. He, K. Gao, S. Zhu, J. Cui, L. Huang, Y. Zhu and Y. Zhao, Catalytic hydrogenation of furfural over Cu/CeO_2 Catalyst: The effect of support morphology and exposed facet, *Appl. Surf. Sci.*, 2022, **604**, 154472.

62 N. Xi, S. Chen, R. Bao, Q. Wang, Y. Lin, J. Yue, R. Wang, C. Yang, W. Yin and T. Qiu, Layered carbon encapsulated CuO_x nanoparticles for selective hydrogenation of furfural to furfuryl alcohol, *Mol. Catal.*, 2024, **565**, 114364.

63 Y. Ren, Y. Yang, L. Chen, L. Wang, Y. Shi, P. Yin, W. Wang, M. Shao, X. Zhang and M. Wei, Synergetic effect of Cu^0-Cu^+ derived from layered double hydroxides toward catalytic transfer hydrogenation reaction, *Appl. Catal., B*, 2022, **314**, 121515.

64 F. Zaccheria, N. Scotti, M. Marelli, R. Psaro and N. Ravasio, Unravelling the properties of supported copper oxide: can the particle size induce acidic behaviour?, *Dalton Trans.*, 2013, **42**(5), 1319–1328.

65 Y. Li, Q. Shen, Y. Nian, F. Wang, X. Zhang, Z. Zhang, C. Bing, X. Fan and R. Ahishakiye, Promoting effect of oxygen vacancies in Co/$CoAl_2O_4$ catalyst steered with a straightforward method on hydrogenation of furfural to 2-methylfuran, *Appl. Catal., B*, 2024, **343**, 123529.

66 S. C. Chou, C. T. Yeh and T. H. Chang, Adsorption of Hydrogen on Dispersed Copper-Rhodium Bimetallic Crystallites, *J. Phys. Chem. B*, 1997, **101**(30), 5828–5833.

67 F. Xu, W. An, A. E. Baber, D. C. Grinter, S. D. Senanayake, M. G. White, P. Liu and D. J. Stacchiola, Enhanced oxide reduction by hydrogen at cuprous oxide-copper interfaces near ascending step edges, *J. Phys. Chem. C*, 2022, **126**(44), 18645–18651.

68 X. G. Wang, J. R. Smith and M. Scheffler, Adhesion of copper and alumina from first principles, *J. Am. Ceram. Soc.*, 2003, **86**(4), 696–700.

69 H. Niu, Y. Cheng, C. Li, S. Li, J. Luo and C. Liang, Construction of Cu-MO_x (M= Zn or Al) interface in Cu catalysts for hydrogenation rearrangement of furfural, *Ind. Eng. Chem. Res.*, 2021, **60**(47), 16939–16950.

70 N. Wang, Y. Quan, J. Zhao, H. Li and J. Ren, Highly active CuZn/SBA-15 catalyst for methanol dehydrogenation to methyl formate: Influence of ZnO promoter, *Mol. Catal.*, 2021, **505**, 111514.

71 U. R. Pillai and S. Deevi, Copper-zinc oxide and ceria promoted copper-zinc oxide as highly active catalysts for low temperature oxidation of carbon monoxide, *Appl. Catal., B*, 2006, **65**, 110–117.

72 L. Ban, H. Li, Y. Zhang, R. Wu, X. Huang, J. H. Zhao and Y. X. Zhao, Importance of zinc oxide in Cu-based catalysts for the ethynylation of formaldehyde to 1,4-Butynediol, *J. Phys. Chem. C*, 2021, **125**(30), 16536–16549.

73 B. R. Strohmeier and D. M. Hercules, Surface spectroscopic characterization of the interaction between zinc ions and γ-alumina, *J. Catal.*, 1984, **86**(2), 266–279.

74 R. M. Palomino, P. J. Ramírez, Z. Liu, R. Hamlyn, I. Waluyo, M. Mahapatra, I. Orozco, A. Hunt, J. P. Simonovis, S. D. Senanayake and J. A. Rodriguez, Hydrogenation of CO_2 on ZnO/Cu (100) and ZnO/Cu (111) catalysts: role of copper structure and metal–oxide interface in methanol synthesis, *J. Phys. Chem. B*, 2018, **122**(2), 794–800.

75 W. Jeon, C. Ban, J. E. Kim, H. C. Woo and D. H. Kim, Production of furfural from macroalgae-derived alginic acid over Amberlyst-15, *J. Mol. Catal. A:Chem.*, 2016, **423**, 264–269.

76 J. Zhang, Z. Jia, S. Yu, S. Liu, L. Li, C. Xie, Q. Wu, Y. Zhang, H. Yu, Y. X. Liu, J. Pang and Y. Liu, Regulating the Cu^0-Cu^+ ratio to enhance metal-support interaction for selective hydrogenation of furfural under mild conditions, *Chem. Eng. J.*, 2023, **468**, 143755.

77 R. Tu, K. Liang, Y. Sun, Y. Wu, W. Lv, C. Q. Jia, E. Jiang, Y. Wu, X. Fan, B. Zhang, Q. Lu, B. S. Zhang and X. Xu, Ultra-Dilute high-entropy alloy catalyst with core-shell structure for high-active hydrogenation of furfural to furfuryl alcohol at mild temperature, *Chem. Eng. J.*, 2023, **452**, 139526.

78 W. Chen, Q. Peng, G. Fan, Q. Cheng, M. Tu and G. Song, Catalytic transfer hydrogenation of furfural to furfuryl alcohol over Al-containing ferrihydrite, *J. Ind. Eng. Chem.*, 2023, **119**, 574–585.

79 J. J. Musci, M. Montaña, A. B. Merlo, E. Rodríguez-Aguado, J. A. Cecilia, E. Rodriguez-Castellon, I. D. Lick and M. L. Casella, Supported ruthenium catalysts for the aqueous-phase selective hydrogenation of furfural to furfuryl alcohol, *Catal. Today*, 2022, **394**, 81–93.

80 W. Mao, J. Liu, B. Yin, D. Kong, S. Miao and F. Wang, Transfer hydrogenation of furfural catalyzed by multi-centers collaborative Ni-based catalyst and kinetic research, *Appl. Catal., A*, 2021, **623**, 118247.

81 F. Li, S. Jiang, J. Huang, Y. Wang, S. Lu and C. Li, Catalytic transfer hydrogenation of furfural to furfuryl alcohol over a magnetic Fe_3O_4@C catalyst, *New J. Chem.*, 2020, **44**(2), 478–486.

82 B. Gao, J. Zhang and J. H. Yang, Bimetallic Cu-Ni/MCM-41 catalyst for efficiently selective transfer hydrogenation of furfural into furfural alcohol, *Mol. Catal.*, 2022, **517**, 112065.

83 P. Weerachawanasak, P. Krawmanee, W. Inkamhaeng, F. J. C. S. Aires, T. Sooknoi and J. Panpranot, Development of bimetallic Ni-Cu/SiO_2 catalysts for liquid phase selective hydrogenation of furfural to furfuryl alcohol, *Catal. Commun.*, 2021, **149**, 106221.